14th International Symposium on Turbulence and Shear Flow Phenomena (TSFP14)
Heidelberg, Germany, July 28–31, 2026

ADAPTIVE WAVELET SIMULATIONS OF THE WAKE BEHIND A FRACTAL TREE WITH APPLICATION TO FLAPPING INSECT FLIGHT

Julius Bergmann
Department of Numerical Fluid Dynamics
Technical University Berlin
Müller-Breslau-Straße 15, 10623 Berlin, Germany
julius.bergmann@univ-amu.fr

Thomas Engels
Institut des Sciences du Mouvement
Centre national de la recherche scientifique
163 Avenue de Luminy, 13009 Marseille, France
thomas.engels@univ-amu.fr

Angela Busse
Department of Numerical Fluid Dynamics
Technical University Berlin
Müller-Breslau-Straße 15, 10623 Berlin, Germany
angela.busse@tu-berlin.de

Kai Schneider
Institut de Mathématiques de Marseille
Aix-Marseille Université, CNRS
3 Place Victor Hugo Case, 13331 Marseille, France
kai.schneider@univ-amu.fr

ABSTRACT

Complex geometries can give rise to strongly non-homogeneous turbulence. Using the wavelet-adaptive solver WABBIT (Engels *et al.*, 2022), we study the wake shed by a fractal tree, extending the fixed-grid simulations of Yin *et al.* (2025*b*). Through wavelet-based grid adaptation, our solver concentrates resolution in regions with fine-scale flow structures, yielding results consistent with the reference data while using significantly fewer grid points. For the Reynolds numbers considered, the fractal tree serves as a generalized model for trees, shrubs, or plants that are encountered by foraging insects. Two-dimensional cuts of the flow and corresponding local wavelet spectra in the wake reveal a strong inhomogeneity of the flow. The bottom of the tree acts as an inhomogeneous cylinder flow with more pronounced turbulence intensity at coarser scales, while the smaller branches of the crown develop more fine-scale turbulence. Insects can thus encounter significantly different plant-wake characteristics depending on which part of a plant they approach.

INTRODUCTION

Trees and shrubs generate complex wake turbulence due to their complex geometry. Although many studies on tree aerodynamics have focused on investigating their drag and porosity properties, little research has been conducted on their wake characteristics. Since insects fly around and between plants on foraging tours, studying the wake dynamics of plants gives important insight into the flight conditions encountered by insects. While the flight characteristics of bumblebees in flow with isotropic turbulence of high turbulence intensity were found to be only marginally affected (Engels *et al.*, 2016, 2019), larger-scale dynamics are known to impact insect flight, especially in unsteady wakes (Engels *et al.*, 2019; Ravi *et al.*, 2013).

Trees, due to their complex branching, can be idealized as fractal trees. Turbulence generated by fractal square grids exhibits non-equilibrium dissipation properties (Hurst & C.Vassilicos, 2007; Vassilicos, 2015). In the study of Yin *et al.* (2025*b*,*a*), similar characteristics were found for fractal trees from centerline results. Based on cross-stream-averaged results measured at different heights for the turbulence intensity and Taylor-microscale-based Reynolds number, Yin *et al.* (2025*b*) argue the generality of their centerline results. However, the profiles shown in their work exhibit two distinct regions, the wake of the main trunk and the tree canopy itself.

This investigation aims to reproduce and extend the results of Yin *et al.* (2025*b*). Spectral analysis using wavelet scalograms of the inhomogeneous wake is undertaken to discern the validity of the results as adaptive DNS as well as differentiate flow characteristics at different Reynolds numbers and between the tree crown and trunk wake. In future work, the results will be extended to a bumblebee and a butterfly flying through the wake towards the tree in flapping flight, linking the wake-study of the fractal tree with the work of Engels *et al.* (2019) on flapping flight in strong turbulence.

METHODOLOGY

The fractal tree is modeled as an L-system (Prusinkiewicz *et al.*, 1996), making it easily replicable. The geometry chosen for the present study was proposed in Yin *et al.* (2025*b*); it is composed of cylinders, starting with the main trunk. At the end of each cylinder, two new elements branch off at a given angle, with the cylinder diameter and length reduced by a factor of 0.8. This process is repeated until a maximum branching depth of n = 4, 6 or 8 is reached, yielding three distinct tree models (Figure 1). The first cylinder length is $L_0 = [0.357, 0.289, 0.257]$ and its diameter is $D_0 = [0.107, 0.087, 0.077]$, chosen such that $H = 1$, where H is the height of the tree. In the context of this work, all length scales are given in units of the tree height H, all velocities as multiples of the freestream velocity $U_\infty = 1$ and time scales are normalized by H/U_∞. Two values of the Reynolds number are considered in this study, $Re = U_\infty H/\nu = 10{,}000$ and $120{,}000$. The tree is placed in a domain of size 32^3 with the tree located at $(8, 16, 16)$ and periodic boundary conditions used in all three spatial directions. In- and outflow boundary conditions are modeled with sponge layers of width 4. The numerical simulations are carried out using our wavelet-adaptive code WABBIT

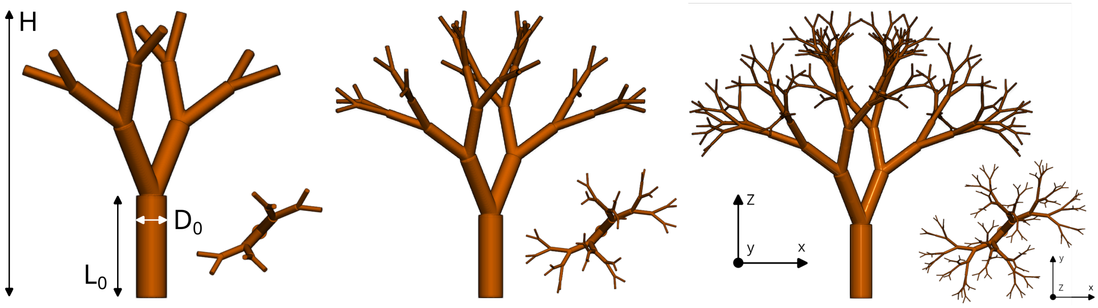

Figure 1: Side-view of the tree geometry for $n = 4$ (left), $n = 6$ (center) and $n = 8$ branches (right). Small insets show top-view of the tree. The inflow U_∞ is in positive x-direction.

(Engels *et al.*, 2022). Using the Multi-Resolution-Analysis (MRA) framework (Farge *et al.*, 1992) together with the volume penalization method as an immersed boundary method, the computational grid is created and adapted automatically to accuracy requirements, enabling dynamic simulations of the wake behind the complex geometry.

The domain is decomposed into a graded octree grid, where each entity is a uniform grid with a block size of 18^3. On this grid, the incompressible Navier–Stokes equations for the velocity $\underline{u}$ and pressure p (setting unit density, $\rho = 1$) are approximated with the artificial compressibility method (ACM) (Ohwada & Asinari, 2010),

$$\partial_t \underline{u} + \frac{1}{2}(\underline{u}\cdot\nabla + \nabla\cdot\underline{u})\underline{u} + \nabla p - \nu\nabla^2\underline{u} + \frac{\chi}{C_\eta}(\underline{u} - \underline{u}_s) = 0\,, \quad (1)$$

$$\partial_t p + C_0^2 \nabla\cdot\underline{u} = 0\,. \quad (2)$$

This relaxes the incompressibility condition by introducing a finite artificial speed of sound C_0, which is set as $Ma = \frac{U_\infty}{C_0} = 0.1$, where U_∞ is the inflow velocity, to achieve nearly incompressible conditions. The ACM formulation benefits from requiring no solution of a Poisson problem. The system is discretized in time using a fourth order Runge–Kutta method; spatial derivatives are discretized using classical, fourth order, centered finite difference stencils.

The fractal tree is modeled with an immersed boundary method (see e.g., Schneider (2015)). Here we use the volume penalization method, which is particularly attractive for high Reynolds number flows. A mask function χ describes the geometry of the tree (Angot *et al.*, 1999), where $\chi = 1$ inside the solid and 0 elsewhere; at the interface, χ is smoothed over a few grid points. During the simulation, blocks containing the actual tree are always kept at the highest refinement level allowed (i.e., the highest resolution), where the grid spacing is Δx_{min}. The penalization parameter, physically interpreted as permeability, is set as $C_\eta = (K_\eta \Delta x_{min})^2/\nu$, with a constant $K_\eta = 0.1$ for the lower and $K_\eta = 0.03$ for the higher Reynolds number case (Nguyen van yen *et al.*, 2014). The solid velocity $\underline{u}_s$ of the tree is zero for all cases.

The numerical grid is dynamically adapted during the simulation using bi-orthogonal Cohen–Daubechies–Feauveau (CDF) wavelets (Cohen *et al.*, 1992). These wavelets are the building blocks for the multiresolution analysis (MRA) framework in order to refine or coarsen individual blocks of the adaptive grid and we use wavelets with fourth-order interpolation. Additionally, wavelets can encode the local details at a specific refinement level as wavelet coefficients, which serve as error estimates when assessing the accuracy of the grid resolution.

During each time-step, the refine-evolve-coarsen procedure is applied (Liandrat & Tchamitchian, 1990). Firstly, the whole grid is refined by a factor of two and then evolved for one time-step. Afterwards, the grid is adapted and blocks containing no significant wavelet coefficient above the adaptation threshold C_ε are coarsened, while the rest is kept at that refinement level. This ensures that all possible scales present in the flow are adequately resolved. However, in practice a maximum refinement level J with resolution Δx_{min} for the grid needs to be imposed for computational reasons, and all blocks at that level are not further refined. The simulation parameters C_0, C_ε and C_η are chosen so that the compressibility, adaptivity, and volume penalization errors are balanced. A detailed explanation and validation of the simulation framework can be found in Engels *et al.* (2022) and a review on adaptive wavelet methods for CFD is given in Schneider & Vasilyev (2010).

	$n=4$	$n=6$	$n=8$
$1/\Delta x_{min} = 144$	0.982	1.160	
$1/\Delta x_{min} = 288$	0.859	1.030	1.158
$1/\Delta x_{min} = 576$	0.786	0.922	1.04
$1/\Delta x_{min} = 1152$	0.762	0.883	0.970
$1/\Delta x_{min} = 2304$		0.857	0.947

Table 1: Averaged drag coefficients for $Re = 10{,}000$.

	$n=4$	$n=6$	$n=8$
$1/\Delta x_{min} = 144$	1.053	1.261	
$1/\Delta x_{min} = 288$	0.869	1.026	1.155
$1/\Delta x_{min} = 576$	0.792	0.909	0.998
$1/\Delta x_{min} = 1152$	0.781	0.843	0.885
$1/\Delta x_{min} = 2304$		0.816	0.827
Yin *et al.* (2025*b*)	0.704	0.747	0.765

Table 2: Averaged drag coefficients for $Re = 120{,}000$. The last line contains values reported by Yin *et al.* (2025*b*) at resolution $1/\Delta x_{min} = 2048$.

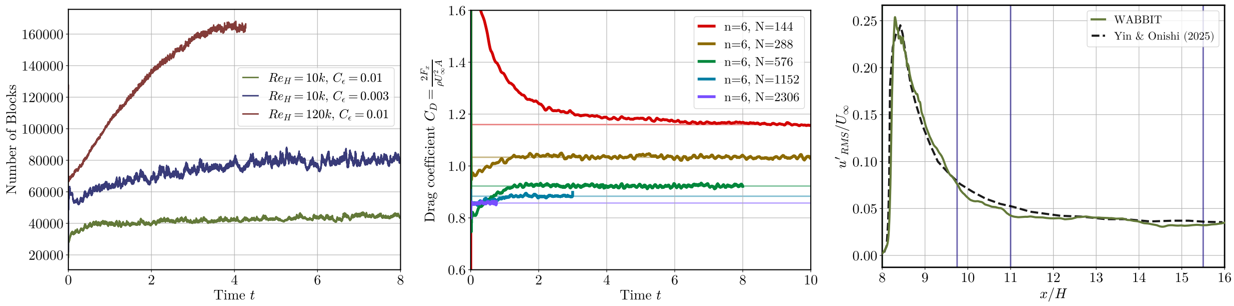

(a) Number of uniform blocks of the adaptive grid over time for the different runs being initialized from results with $C_\varepsilon = 0.1$.

(b) Drag coefficient C_D of the fractal tree over time for $Re_H = 10{,}000$ and $n = 6$. The horizontal lines depict the values averaged over the last interval of $\Delta t = 1$.

(c) Centerline turbulence intensity $\frac{u'_{RMS}}{U_\infty}$ at $y = 16$, $z = 16.5$ for $C_\varepsilon = 0.01$ together with data extracted from Yin *et al.* (2025*b*) for $Re_H = 10{,}000$. At the vertical lines, the adaptive grid is coarsened by a factor of two.

Figure 2: Adaptive grid size (a) and grid convergence of drag coefficients (b) over time, as well as centerline turbulence intensity along the wake.

INVESTIGATIONS

In order to determine the adequate resolution of the geometry, the grid dependency of drag coefficients is analyzed and validated against the results reported by Yin *et al.* (2025*b*). The drag coefficient is defined as $C_D = \frac{2F_x}{\rho U_\infty^2 A}$. Here, F_x is the force in the streamwise direction. The normalized area of the tree projected on the y-z plane is $A = [0.1396, 0.1524, 0.1749]$ for the three models, respectively. Preliminary results showed that the details of the wake dynamics do not affect the drag coefficient. Hence, the drag is insensitive to the choice of wavelet or wavelet threshold C_ε, but is mainly influenced by the maximum grid resolution. The grid-dependency study has therefore been conducted with the computationally more efficient unlifted CDF40 wavelet, as well as a large threshold of $C_\varepsilon = 0.1$. Due to the large adaptation threshold, the grid quickly coarsens behind the tree and the simulations act as implicit LES, i.e., the wake turbulence is not fully resolved. We first run the coarsest resolution until $t = 10$ to pass the initial transient. Afterwards, the last snapshot is used as initial condition for a simulation where the maximum resolution is increased by a factor of two, and this new simulation is run until the drag coefficient is fully developed. This procedure is repeated for successively finer maximum resolutions. In each case, drag coefficient values are averaged over the last available interval of length $\Delta t = 1$.

Results for C_D are given in Table 1 for $Re = 10{,}000$ and Table 2 for $Re = 120{,}000$. The behavior of C_D over time for the case $n = 6$ and $Re = 10{,}000$ is shown in Figure 2b. Overall, the drag coefficients show a general convergence to a grid-independent solution, but a slower convergence in comparison to Yin *et al.* (2025*b*) can be observed, which is likely due to the first order approximation of the volume penalization method. The values for the maximum resolution computed with WABBIT are around 10% higher than those reported in Yin *et al.* (2025*b*). The drag coefficients reported for both the $Re = 10{,}000$ case and $Re = 120{,}000$ case are very similar for the lower maximum branch depths $n = 4$ and $n = 6$. For $n = 8$ the drag values differ significantly between the two Reynolds numbers, although these differences can be observed only at the higher resolutions. The flow effect of the fine branches requires a resolution of at least $1/\Delta x_{min} = 1152$ at $Re = 120{,}000$. For the maximum resolution of $1/\Delta x_{min} = 2304$, the smallest branch diameters are resolved with $D_{min}/\Delta x_{min} = [87.2, 35.32, 15.76]$ for the three maximum branching depths of $n = [4, 6, 8]$, respectively.

In the main study with refined wake structures we focus on the case $n = 6$ employing a maximum resolution of $1/\Delta x_{min} = 576$. This tree configuration was chosen since available computational resources did not allow for sufficient resolution and sampling time in the $n = 8$ case. Several computations were performed with a smaller adaptation threshold to further analyze the resulting turbulent wake of the tree. The threshold is set to $C_\varepsilon = 0.01$ and simulations are run for both Reynolds number cases. For these simulations we are using the lifted wavelet CDF42 to ensure an adequate representation of the wake even on coarser resolutions. Simulations are initialized with a larger $C_\varepsilon = 0.1$, before lowering it to the desired value and continuing the runs for sufficient flow through the domain. The grids have on average around $45{,}000$ blocks or 262 million grid points for the lower, and around $163{,}000$ or 950 million grid points for the higher Reynolds number and stay relatively constant over time, once the refinement of the wake structure has developed (see Figure 2a). An additional simulation for the lower Reynolds number with lower adaptation threshold of $C_\varepsilon = 0.003$ is performed to investigate the independency of the results from the choice of threshold C_ε.

The time-averaged mean flow avg($\underline{u}$) as well as variance var($\underline{u}$) are computed based on running averages over the simulation, meaning that they undergo the same refine-evolve-coarsen cycle as the state variables. Due to the smooth nature of these variables, the continuous filter applications of the multi-resolution-analysis are not found to significantly affect the time-averaged quantities. The turbulence intensity I can be computed as

$$I = \frac{u'_{RMS}}{U_\infty} = \frac{\sqrt{\frac{1}{3}\left(\mathrm{var}(u_x) + \mathrm{var}(u_y) + \mathrm{var}(u_z)\right)}}{U_\infty}. \quad (3)$$

For the lower Reynolds number simulations, statistics are averaged over an interval of length $\Delta t = 5$. Results for the centerline turbulence intensity for averaging duration of $\Delta t = 3$ and $\Delta t = 5$ coincided, justifying that $\Delta t = 5$ is sufficient. To validate against the reference results from Yin *et al.* (2025*b*), the turbulence intensity along the predefined centerline is compared and shown in Figure 2c. This centerline is situated at $y = 16$ and $z = 16.5$ in the center of the tree profile and captures the general dynamics of the turbulence intensity along the wake. Even with changes in resolution for the adaptive grid, the results agree well with those of the reference.

2D cuts of the instantaneous vorticity along the x-z direction at the tree center ($y = 16$) are given in Figure 4 for both Reynolds numbers. The visible front part of the tree illustrates its asymmetry against the inflow direction. The vorticity cut depicts the turbulent wakes shed behind the tree branches, with some branches barely piercing the vorticity cut-plane. The wake of the main tree trunk is especially pronounced, and a strong vortex is being shed from just above the first branching point, which passes the centerline (depicted in red), being the main reason for all the centerline peaks reported by Yin *et al.* (2025*b*). We overlay the adaptive computational grid of uniform blocks, which follows the tree geometry and main wake region. For $Re = 10,000$, the structures in the wake quickly decay and the grid starts to coarsen, while for $Re = 120,000$ the grid stays refined at the maximum grid resolution due to pronounced fine-scale structures.

The wake can be further analyzed in wavelet space considering the velocity field at individual scales 2^{-j}. To this end, the velocity is wavelet-decomposed using CDF44 wavelets. Summing the squares of all wavelet coefficients at a given scale yields the so-called energy-scalogram, E_j at scale 2^{-j} (Meneveau, 1991; Farge *et al.*, 1992). Note that the energy is normalized by the domain volume and thus results are shown for the specific energy. The scale 2^{-j} can be related to the mean wavenumber $k_j = k_\psi 2^j$ of the wavelet, where k_ψ is its centroid wavenumber, $k_\psi = 0.84$ for CDF44. Dividing E_j by the wavenumber range $2\Delta k_j = 2(k_{j+1} - k_j)\ln 2$, we obtain the wavelet energy spectrum which is a smoothed version of the Fourier energy spectrum. With CDF44, the wavelet spectrum can detect power laws up to k^{-9}, see e.g., (Schneider *et al.*, 2004). To neglect the effect of the mean flow, the wavelet spectrum is computed using instantaneous fluctuations $\underline{u}'(t) = \underline{u}(t) - \mathrm{avg}(\underline{u})$ from one snapshot. Moreover, wavelets offer the possibility to quantify the scale distribution of energy locally Farge *et al.* (1992). We compute local wavelet energy spectra by only computing the energy in parts of the domain, for instance in the wake of the fractal tree considering different downstream distances. To this end, we use slices of thickness $32/(18 \cdot 2)$ in the x-direction for different downstream positions.

The local wavelet spectra can be found in Figure 3. Intervals containing the tree geometry have energy mostly present in fine scales and energy peaks around the wavenumber for the tree trunk diameter $2\pi/D_0 \approx 72$ (figure 3a). Already there, the rapid decay of the spectra due to dissipation is visible with no distinct inertial range. For increasing downstream positions, the energy peak is moving towards smaller wavenumbers as vortex structures created from the small branches start to merge. The wavelet spectra computed with different adaptation thresholds C_ε collapse even far downstream in the wake, indicating that the choice of $C_\varepsilon = 0.01$ is sufficient for adaptive DNS simulations to adequately represent the wake characteristics at the lower Reynolds number (figure 3b). Therefore, the observed rapid decay is not originating from the numerical dissipation when adapting the grid. The local wavelet spectra with higher Reynolds number show similar behavior at coarse scales with a clear inertial range over an order of magnitude in wavenumber. These, however, do not initially feature a dissipative range indicated by a rapid decay in the spectra. Hence, it cannot be clearly asserted wether the dissipation at later positions is driven by the physical dissipation or the numerical dissipation from the grid adaptation itself. Simulations with a higher resolution of the wake would be needed to validate the results as an adaptive DNS. For coarse scales, the local wavelet spectra for both Reynolds number cases coincide, so that the effect of the lower viscosity does not significantly affect the large-scale dynamics of the flow.
When separating the wake into a top part from the crown and a bottom part from the tree trunk, the individual contributions show energy distributions (figure 3c), with the wake of the trunk having its energy peak at lower wavenumbers and the wake of the tree crown having more energy present in fine scales. This means that the turbulence within the wake is changing at different heights and analyzing the wake dynamics at certain locations, i.e., the centerline, will not capture the full inhomogeneity of the fractal tree wake.

CONCLUSIONS

We simulated the wake behind a fractal tree geometry using our wavelet adaptive solver WABBIT, which embeds the tree geometry into a graded octree grid and automatically adapts the grid resolution to local flow structures and the geometry. The drag coefficient converged to values close to that of Yin *et al.* (2025*b*) for different tree branch depths, as well as Reynolds numbers $Re = [10,000; 120,000]$. Several simulations with grid refinement were performed for a maximum tree branch depth $n = 6$ with a lower adaptation threshold C_ε, where the developing wake is kept at higher resolution, acting as an adaptive DNS. The turbulence intensity along the centerline for $Re = 10,000$ agreed well with the reference in Yin *et al.* (2025*b*). Local wavelet spectra allowed for further spectral investigation of the fractal tree wake. They revealed that the wake for the case $Re = 10,000$ was sufficiently resolved with $C_\varepsilon = 0.01$ as well as maximum resolution of $1/\Delta x_{min} = 576$. The initial energy distribution showed no clear inertial range, and the energy peak moved to coarser scales along the wake. Preliminary wavelet spectra results for the higher Reynolds number did not show sufficient rapid decay of the spectra at this resolution and a wake resolution larger than $1/\Delta x_{min} = 576$ will be required to fully resolve all wake dynamics. Nevertheless, the local energy spectra for coarse scales coincided between the two Reynolds number studied. We also found a different energy distribution when evaluating the local wavelet spectra on only the top or bottom part of the tree wake, highlighting the inhomogeneity of the flow.

This study serves as the foundation for simulations of insects, notably bumblebees and butterflies, in the wake of the tree. When choosing a bumblebee characteristic size as that of the tree trunk diameter, similar to work done by Ravi *et al.* (2013), the resulting Reynolds number for the fractal tree is between the two investigated here for a typical cruising speed. Even though the branches of the crown are substantially smaller, the shift of the maximum energy to smaller wavenumbers should affect the insects at a size relative to the main tree trunk. We aim to insert different insects at positions within the wake of the tree trunk and crown in order to investigate the effects of the inhomogeneous wake on the flight capabilities.

ACKNOWLEDGEMENTS

Funding by DFG-ANR, project CVS-FIT (ANR-23-CE46-0014-02, DFG 529979103) is gratefully acknowledged. The authors were granted access to the HPC resources of IDRIS and IRENE under allocation No. A0182A14152 attributed by Grand Équipement National de Calcul Intensif (GENCI). The authors were granted access to the HPC resources of Centre de Calcul Intensif d'Aix-Marseille Univer-

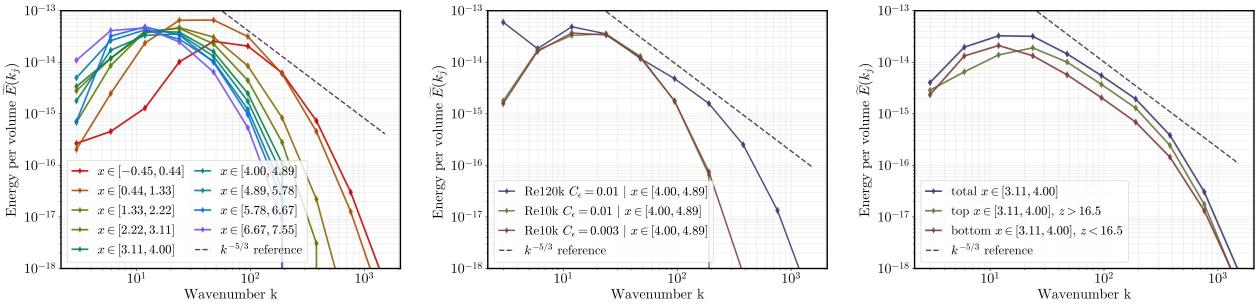

(a) Local wavelet spectra of slices perpendicular to the downstream direction for $Re_H = 10{,}000$ and $C_\varepsilon = 0.01$ at different downstream intervals $x \in [a,b]$ of the same thickness.

(b) Local wavelet spectra of a slice in the interval $x \in [4.00, 4.89]$ perpendicular to the downstream direction for different Reynolds numbers and adaptation thresholds.

(c) Local wavelet spectra of a slice in interval $x \in [3.11, 4.00]$ perpendicular to the downstream direction for $Re_H = 120{,}000$ together with contributions from the top and bottom half of the slice.

Figure 3: Local wavelet spectra in slices perpendicular to the downstream direction.

sité.

REFERENCES

Angot, P., Bruneau, C. & Fabrie, P. 1999 A penalization method to take into account obstacles in incompressible viscous flows. *Numer. Math.* **81**, 497–520.

Cohen, A., Daubechies, I. & Feauveau, J. C. 1992 Biorthogonal bases of compactly supported wavelets. *Comm. Pure Appl. Math.* **45**, 485–560.

Engels, T., Kolomenskiy, D., Schneider, K., Farge, M., Lehmann, F.-O. & Sesterhenn, J. 2019 Impact of turbulence on flying insects in tethered and free flight: High-resolution numerical experiments. *Phys. Rev. Fluids* **4**, 013103.

Engels, T., Kolomenskiy, D., Schneider, K., Lehmann, F.-O. & Sesterhenn, J. 2016 Bumblebee flight in heavy turbulence. *Phys. Rev. Lett.* **116**, 028103.

Engels, T., Truong, H., Farge, M., Kolomenskiy, D. & Schneider, K. 2022 Computational aerodynamics of insect flight using volume penalization. *C. R. Méc.* **350**, 131–150.

Farge, M., Goirand, E., Meyer, Y., Pascal, F. & Wickerhauser, M. V. 1992 Improved predictability of two-dimensional turbulent flows using wavelet packet compression. *Fluid Dynamics Research* **10**, 229–250.

Hurst, D. & C.Vassilicos, J. 2007 Scalings and decay of fractal-generated turbulence. *Phys. Fluids* **19** (3), 035103.

Liandrat, J. & Tchamitchian, P. 1990 Resolution of the 1d regularized burgers equation using a spatial wavelet approximation. *Tech. Rep.*.

Meneveau, C. 1991 Analysis of turbulence in the orthonormal wavelet representation. *Journal of Fluid Mechanics* **232**, 469–520.

Nguyen van yen, R., Kolomenskiy, D. & Schneider, K. 2014 Approximation of the Laplace and Stokes operators with Dirichlet boundary conditions through volume penalization: A spectral viewpoint. *Numer. Math.* **128**, 301–338.

Ohwada, T. & Asinari, P. 2010 Artificial compressibility method revisited: Asymptotic numerical method for incompressible Navier–Stokes equations. *J. Comput. Phys.* **229**, 1698–1723.

Prusinkiewicz, P., Hammel, M., Hanan, J. & Mech, R. 1996 L-systems: from the theory to visual models of plants .

Ravi, S., Crall, J.D., Fisher, A. & Combes, S. A. 2013 Rolling with the flow: bumblebees flying in unsteady wakes. *J. Exp. Biol.* **216**, 4299–4309.

Schneider, K. 2015 Immersed boundary methods for numerical simulation of confined fluid and plasma turbulence in complex geometries: a review. *J. Plasma Phys.* **81**, 435810601.

Schneider, K., Farge, M. & Kevlahan, N. 2004 Spatial intermittency in two–dimensional turbulence: a wavelet approach. In *Woods Hole Mathematics, Perspectives in Mathematics and Physics* (ed. N. Tongring & R.C. Penner), , vol. 34, pp. 302–328. World Scientific.

Schneider, K. & Vasilyev, O. 2010 Wavelet methods in computational fluid dynamics. *Annu. Rev. Fluid Mech.* **42**, 473–503.

Vassilicos, J. C. 2015 Dissipation in turbulent flows. *Annual Review of Fluid Mechanics* **47** (Volume 47, 2015), 95–114.

Yin, Y., Onishi, R., Watanabe, S., Segrovets, I., Nagata, K. & Aoki, T. 2025*a* Non-equilibrium dissipation in paired fractal-tree turbulence. *Physics of Fluids* **37** (8), 085233.

Yin, Y., Onishi, R., Watanabe, S., Segrovets, I., Nagata, K. & Aoki, T. 2025*b* Numerical study of fractal-tree-generated non-equilibrium turbulence. *Journal of Fluid Mechanics* **1007**, A45.

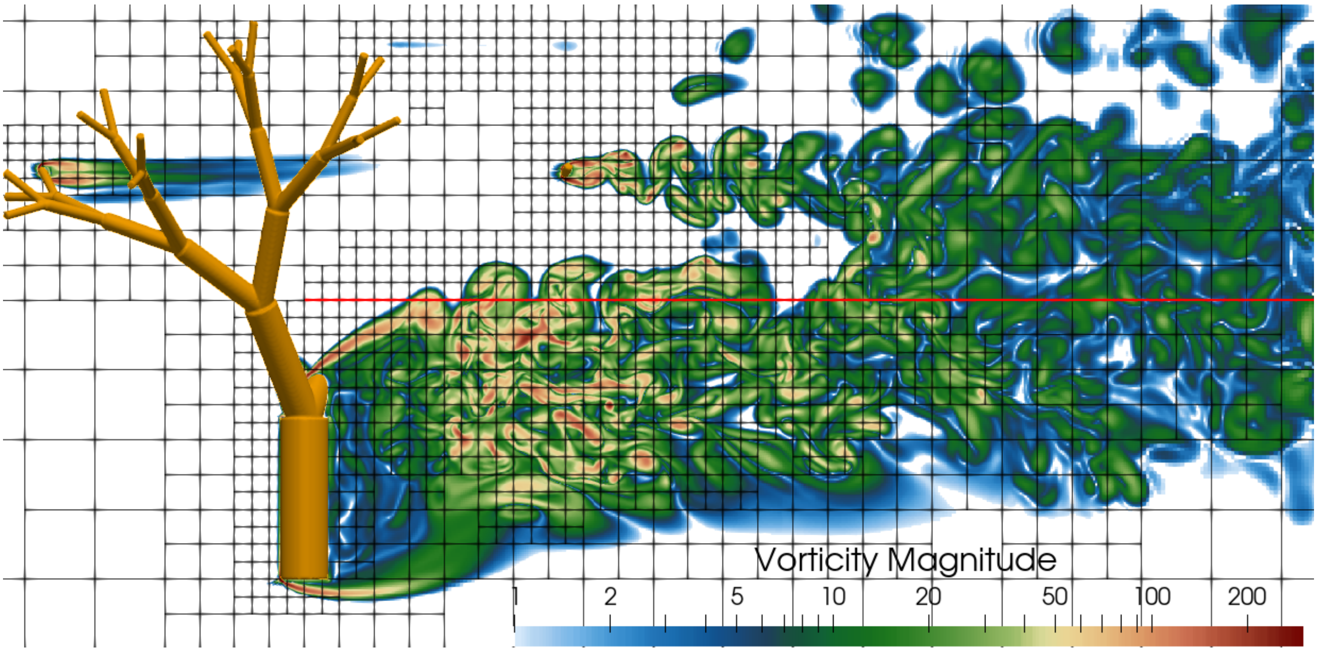

(a) $Re_H = 10,000$

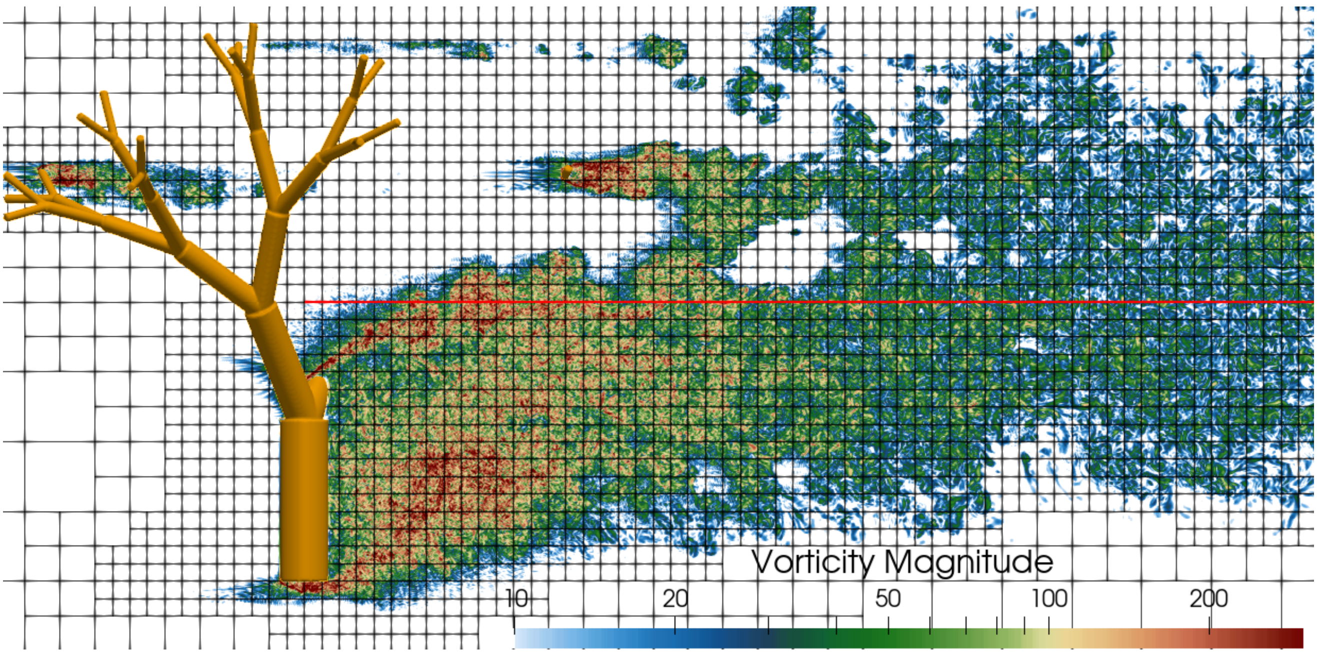

(b) $Re_H = 120,000$

Figure 4: Fractal tree geometry with maximum branch depth $n = 6$, together with a y-z cut showing the instantaneous vorticity magnitude $|\underline{\omega}|$ and octree grid of uniform blocks for both Reynolds number cases. Depicted in red is the position of the centerline, defined in the text. Note that the color tables are different and have been adapted to visualize the relevant flow structures.